Materials Horizons

ROYAL SOCIETY OF CHEMISTRY

COMMUNICATION

View Article Online
View Journal | View Issue

Cite this: *Mater. Horiz.*, 2023, **10**, 2237

Received 8th February 2023,
Accepted 22nd March 2023

DOI: 10.1039/d3mh00188a

rsc.li/materials-horizons

A highly sensitive friction-imaging device based on cascading stimuli responsiveness†

Nano Shioda,[a] Ryotaro Kobayashi,[b] Seiichiro Katsura,[b] Hiroaki Imai,[a] Syuji Fujii *[c] and Yuya Oaki *[a]

Imaging and measurement of friction forces are required in a variety of fields. If the friction forces originating from the motions of professionals are quantitatively analyzed, the data can be applied to a motion-copying system by a robot. However, weak friction forces have not been visualized and quantified using conventional sensing materials and devices because of their low sensitivity. Here we present a highly sensitive friction-imaging device based on the cascading responses of stimuli-responsive materials, namely polydiacetylene (PDA) and dry liquid (DL). Weak friction forces disrupt the DL, which is composed of liquid droplets surrounded by solid particles. The outflowing liquid under chemical stress changes the color of PDA. The cascading responses enable colorimetric imaging and measurement of weak friction forces in the range of 0.006–0.080 N. Furthermore, the device visualizes the force distribution of handwriting in calligraphy depending on the individual characteristics of an expert, a practician, and a beginner. A high-sensitivity friction-imaging device can be used to understand various motions.

New concepts

We visualize and measure invisible weak frictional forces in the range of 0.006–0.08 N, which were not detected in previous works, without excitation light. A highly sensitive friction-imaging device has been designed using a combination of stimuli-responsive materials and substrates. Although mechanoresponsive materials have been studied in previous works, they meet the limitation for the enhancement of sensitivity. If molecules and their assemblies with high sensitivity are designed, the responses, such as color changes, based on thermal molecular motion will proceed under ambient conditions. Therefore, a new device design is required to sense weak friction forces. In our concept, the weak friction force disrupts a capsule material, which is composed of liquid droplets surrounded by solid particles, on a substrate with appropriate surface roughness. The outflowing interior liquid under chemical stress changes the color of a stimuli-responsive conjugated polymer coated on the substrate. The device visualizes and measures the local distribution of weak friction forces, such as handwriting in calligraphy. The present concept of the device design combining the stimuli-responsive materials and substrates can be applied to the development of various force imaging and sensing devices.

1. Introduction

Friction forces applied between two materials are found in a wide range of lengths and strengths.[1–6] For example, experienced and professional persons apply precisely regulated friction forces on target objects, such as in calligraphy and surgery. If the friction forces are imaged and measured, the data can be used by robots and inheritors to mimic skillful motions. However, friction forces weaker than 1 N, such as those involved in calligraphic writing, have not been visualized and quantified using conventional sensing materials and devices owing to their low sensitivity.[7–20] In the present work, a highly sensitive friction-imaging device was designed based on cascading responses combining two stimuli-responsive materials (Fig. 1). The device exhibits visible color changes without excitation light in response to friction forces in the range of 0.006–0.08 N, which were not detected in previous works (Fig. 1i and Fig. S1 in the ESI†). Moreover, force distribution mapping during calligraphic writing was achieved using this device (Fig. 1h).

Mechanoresponsive materials have been studied for the detection of tensile, frictional, and compressive stresses.[7–20] If the macroscopically applied stresses induce microscopic molecular motion, visible and/or fluorescent color changes can be observed. In general, mechanoresponsiveness has been achieved through the molecular design of materials, such as complexes, liquid crystals, and polymers.[7–20] Friction forces were detected by

[a] *Department of Applied Chemistry, Faculty of Science and Technology, Keio University, 3-14-1 Hiyoshi, Kohoku-ku, Yokohama 223-8522, Japan. E-mail: oakiyuya@applc.keio.ac.jp*
[b] *Department of System Design Engineering, Faculty of Science and Technology, Keio University, 3-14-1 Hiyoshi, Kohoku-ku, Yokohama 223-8522, Japan*
[c] *Department of Applied Chemistry, Faculty of Engineering, Osaka Institute of Technology, 5-16-1 Omiya, Asahi-ku, Osaka 535-8585, Japan. E-mail: syuji.fujii@oit.ac.jp*

† Electronic supplementary information (ESI) available: Experimental methods. Summary of related previous works. Detailed structural analyses of materials and devices. Source data of the device with the application of friction forces. Data of the reference samples. See DOI: https://doi.org/10.1039/d3mh00188a

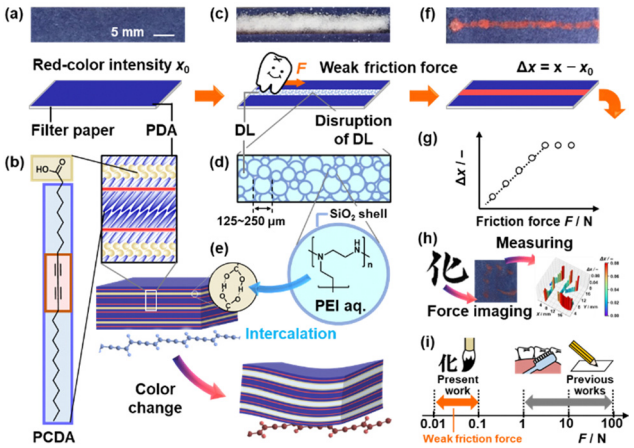

Fig. 1 Imaging and measurement of weak friction forces using a PDA/DL device. (a) A photograph of the PDA-coated filter paper and its illustration. (b) PCDA monomer (left) and its layered crystal structure with the topochemical polymerization of the DA moiety (right). (c) A photograph of the PDA/DL device and its illustration. (d) A schematic illustration of DL and the interior PEI solution surrounded by the shell SiO_2 nanoparticles. (e) Color changes in the layered PDA through the intercalation of PEI flowing out of the disrupted DL. (f) A photograph of the color-changed device and its illustration. (g) The relationship between F and Δx as a standard curve to estimate an unknown F. (h) Imaging and measurement of the force distribution of writing in calligraphy. (i) The detection range of friction forces in the present and previous works.

fluorescent color changes originating from the conformational changes of the chromophore.[21–27] However, quantitative measurements, sensitivity control, and visible color change without the use of excitation light have not been achieved in the previous works. In particular, sensing of weak friction forces lower than 1 N has not been achieved (Fig. S1 in the ESI†). If mechanoresponsive materials with high sensitivity are designed, color changes based on thermal molecular motion will proceed under ambient conditions. Therefore, new design strategies for materials and devices are required to sense weak frictional forces. Here, we combined two stimuli-responsive materials, color-changing PDA and mechanoresponsive capsule DL, on a paper substrate to prepare a PDA/DL device (Fig. 1a–d). The applied weak friction force was initially converted to a chemical stimulus through the disruption of the DL (Fig. 1d and e). The color change of PDA was induced by the chemical stimulus (Fig. 1e and f). The cascading responses enable high-sensitivity imaging and measurement of the friction force (Fig. 1g–i).

PDA is a stimuli-responsive color-changing macromolecule.[28–31] The color of PDA is changed by torsion of the conjugated main chain in response to external stimuli (Fig. 1e), such as heat, light, and force. Responsivity is generally controlled by the design of diacetylene (DA) monomers and their self-organized states.[32–42] Amphiphilic DA monomers such as 10,12-pentacosadiynoic acid (PCDA) form vesicles and layered structures *via* self-assembly (Fig. 1b). Topochemical polymerization provides PDA in the condensed state upon irradiation with UV light. In previous studies, friction forces were visualized by the color changes of PDA.[15,43–50] Our group visualized and quantified friction forces in the range of 0.9–23 N using layered PDA containing interlayer guests.[48,49] However, the design of molecules and materials does not overcome the limitation of low sensitivity. Recently, atomic force microscopy (AFM) has been used to measure the forces required for color changes in PDA.[51,52] Normal and/or friction forces directing conformational changes were measured in nanometer-scale local areas. Although the measured forces in the nN range are apparent in the local area, sensitivity improvement was not achieved in the AFM studies. In the present work, we used DL for cascading responses to improve sensitivity (Fig. 1d). A DL is a free-flowing powder of a liquid droplet surrounded by solid particles.[53,54] As the interior liquid flows out of the DL with the application of weak mechanical stress, the mechanical stress is converted to chemical stress, leading to a color change in PDA. In our previous study,[55] DL was combined with PDA to detect only "compression" stresses. However, the other stresses were not detected using the device with DL. In the present work, DL dispersed on the PDA-coated substrate (PDA/DL) was applied to detect "friction" forces with enhanced sensitivity more than ten times that of the PDA-coated paper device without DL (Fig. 1c–f). The device exhibited a colorimetric response to the applied friction force (Fig. 1g). Furthermore, applied forces including friction and compression stresses, such as handwriting in calligraphy, were visualized using a PDA/DL device (Fig. 1h). The highly sensitive friction-imaging device can be applied to visualize and measure a variety of friction forces originating from motion. A design strategy based on cascading responses can be used to develop other sensing materials and devices.

2. Results and discussion

2.1. PDA/DL paper device and its enhanced responsivity

PDA-coated filter paper and DL were prepared according to the methods described in our previous works.[54,56] The PDA-coated paper was prepared for temperature-distribution imaging.[56] The detailed procedure is described in the ESI.† The PCDA monomer was dip-coated on commercial filter paper and then polymerized under UV irradiation. The filter paper consisted of cellulose fibers 1–10 μm in width (Fig. 2a). After polymerization, the color of the filter paper changed to blue, which is a characteristic of PDA (inset of Fig. 2c). Cellulose fibers were covered with the PDA sheets approximately 1 μm in width and 0.1 μm in thickness on the secondary electron (SE) image by scanning electron microscopy (SEM) (Fig. 2c and Fig. S2 in the ESI†). A back-scattered electron (BSE) image showed a bright contrast domain corresponding to the PDA coating (Fig. 2d), whereas such contrast was not observed on the bare filter paper (Fig. 2b). Raman spectroscopy confirmed the coating of PCDA and its polymerization to PDA (Fig. S2 in the ESI†). DL was prepared by mixing silica (SiO_2) nanoparticles and polyethylenimine (PEI, $\bar{M}_n$ = 300) aqueous solution and then homogeneously dispersing them on the PDA-coated substrate (Fig. 2e–g).[54] An accumulated layer of DL particles with a thickness of *ca.* 500 μm was observed on the PDA-coated substrate by X-ray computed tomography (XCT) (Fig. 2e and f). DL had an average diameter of 140.3 ± 62.6 μm (Fig. 2g and Fig. S3 in the ESI†). Water in DL was gradually evaporated within *ca.* 20 min at room temperature

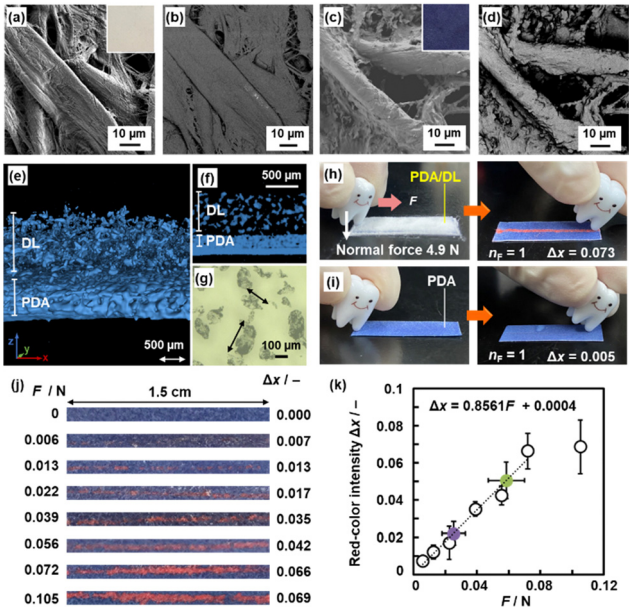

Fig. 2 PDA/DL device and its response to weak frictional forces. (a–d) SE (a and c) and BSE (b and d) images of a filter paper before (a and b) and after (c and d) coating PDA (insets: photographs). (e and f) 3D perspective (e) and cross-sectional (f) XCT images of the PDA/DL device. (g) Optical microscopy image of DLs. (h and i) Photographs of PDA/DL (h) and PDA (i) before (left) and after (right) the application of weak friction forces. (j) Photographs and their Δx with the application of weak friction forces. (k) Relationship between F and Δx as the standard curve (open circles) and estimation of simulated unknown F (green and purple circles).

under ambient pressure. We stored the DL in a sealed plastic bottle after the preparation until use. DLs stored in a plastic bottle can be used anytime. Evaporation of water was not observed in a plastic bottle, whereas DLs are disrupted with the evaporation of water in a glass bottle. The wetting on the hydrophilic surface of glass causes diminishing of smaller water droplets by Ostwald ripening. Therefore, the DL was dispersed on the device just before the application of the friction forces.

The friction force was applied by hand with a glass tooth object and a normal force (N) of 4.9 N (Fig. 2h and i). The remaining DL on the device was removed with air blow using a handy blower to take the photograph for the image analysis. The red color intensity (x) was calculated from the RGB values of the photographs using an international standard (see ESI†).[57] A distinct irreversible color change was observed in the PDA/DL device with the number of one-way sliding (applying) times (n_F) = 1. The increment of x to the initial state ($\Delta x = x - x_0$) was 0.073 at n_F = 1 for the PDA/DL device (Fig. 2h). In contrast, PDA without DL showed color changes of Δx = 0.005 at n_F = 1 and Δx = 0.042 at n_F = 100 (Fig. 2i and Fig. S4 in the ESI†). The sensitivity of PDA/DL was enhanced 14.6 times compared with that of PDA. When the DL and PDA powders were in contact with the electrified polystyrene substrate, the particles were adsorbed on the substrate (Fig. S5 in the ESI†). The disruption of DL and color change of PDA were not observed. The facts imply that the color change of PDA and the disruption behavior of DL are not influenced by the triboelectrification.

The PDA/DL device showed a colorimetric response to friction forces (F) in the range of F = 0.006–0.08 N (Fig. 2j and k). A weight mounted on the base with four legs was prepared and slid one way on the PDA/DL device (Fig. 2j and Fig. S5 in the ESI†). The remaining DLs were removed with air blow using a handy blower. The photographs were taken and then the images in the analyzing area (0.5 mm × 15 mm) without the blue blank space were analyzed to calculate the x value. The overall processes, including the device setting and photograph taking, were carried out within 2 min (Scheme S1 in the ESI†). As the weight in the range of 0–300 g loaded on 18 g of the base was placed in an area of 0.01 cm^2, F in the range of 0.006–0.105 N was applied to the device. The applied N and F were measured to estimate the friction coefficient using a platform scale under the device and spring scales, respectively (Fig. S5 in the ESI†). The red-colored domain of the device increases with increasing F (Fig. 2j). In principle, F and Δx have a linear relationship (Fig. S6 in the ESI†). The relationship between F and Δx was approximated to be linear in the range of 0.006–0.08 N (Fig. 2k and Fig. S7 and Table S1 in the ESI†). On the other hand, the color change was not observed when F lower than 0.006 N, namely 0.002 and 0.004 N, was applied by the different setup (Fig. S7 in the ESI†). F was varied by changing the roughness of the contact area when sandpaper was attached (Fig. S8 and Table S2 in the ESI†). A larger Δx value was observed when the friction coefficient was increased by the sandpaper. The results indicate that the present device measures the applied friction forces. In this manner, the weak friction forces are imaged and colorimetrically measured using Δx. The applied F provides the work (energy) to DL. The disruption of DLs in response to the received work induces the outflow of the interior liquid containing PEI. As the volume of the outflowing liquid increases with an increase in the work, the red-color intensity (Δx) is increased. In this manner, the energy originating from friction force is mainly used for the disruption of DLs leading to the color changes. Furthermore, changes in the particle sizes of DLs and the intercalation of the guests in the interlayer space of PDA tuned the sensitivity by 0.33–1.70 times (Fig. S9, S10 and Tables S3–S5 in the ESI†). When larger DLs (212–300 μm) were used instead of the standard condition (105–250 μm), larger Δx values corresponding to higher sensitivity were achieved under the same F. In contrast, smaller DLs (74–105 μm) lowered the sensitivity (Fig. S9 in the ESI†). Larger DLs disrupt more easily compared with smaller DLs (Fig. S13 in the ESI†). In addition, the sensitivity was lowered by the intercalation of nickel ions (Ni^{2+}) in the layered PDA on the paper substrate. The intercalation of PEI in the outflowing interior liquid is delayed by the already intercalated guests. The friction force was applied using two objects with a distance of 250 μm to study the spatial resolution (Fig. S11 in the ESI†). Although the color-changing area was almost consistent with the stressed area, the red-color domain slightly exuded the unstressed area. According to the average diameter of DLs (*ca.* 140 μm), the spatial resolution was approximately 250 μm on this device.

Simulated unknown friction forces F, namely 0.029 and 0.062 N, were applied by changing the weight in the same setup (colored plots in Fig. 2k and Fig. S12 and Table S6 in the ESI†). The Δx values were estimated from the photographs. The estimated F was 0.025 ± 0.007 N from Δx = 0.022 ± 0.006 and 0.059 ± 0.011 N from Δx = 0.050 ± 0.010 using the standard curve. The actual and estimated F values were consistent with each other. The relationship between F and Δx can be used for the colorimetric estimation of unknown friction forces.

2.2. Cascading responses for enhanced sensitivity of PDA/DL

Enhanced sensitivity was achieved by cascading stimulus responsiveness in the device (Fig. 1 and 3). DL was dispersed on the surface of the PDA-coated paper (Fig. 2e, f and h). At the macroscopic scale, the applied frictional force results in disruption of the DL and outflow of the interior PEI solution on the filter paper. After the collapse of the DLs, fragments of the shell SiO_2 particles were observed in the cellulose fiber network in the SEM image of the red-colored area (area R) (Fig. 3a and b). In addition, Si and N resulting from SiO_2 and PEI were detected in area R by energy dispersive spectroscopy (EDX), respectively (Fig. 3c–f). In contrast, Si and N were not detected in the original blue area (area B) (Fig. 3a–f). A reference colored-DL (c-DL) was prepared by adding a red-colored dye (rhodamine B) to the interior liquid to visualize and estimate the spread with collapse (Fig. S13 and Table S7 in the ESI†). Weak friction forces in the same range were applied to bare filter paper (without PDA coating) with a dispersion of c-DL. The same linear relationship between Δx and F was observed for the reference device in the range of F = 0.006–0.080 N (Fig. S13 in the ESI†). However, the sensitivity of the reference device was 0.053 times lower than that of the PDA/DL device. In addition, the number of collapsed DLs increased with increasing F (Table S8 in the ESI†). These facts indicate that an increase in F induces an increase in the number of collapsed DL and the volume of the outflow PEI solution. A larger F induces the more frequent disruption of DLs with the entanglement by the probe (Fig. S13 in the ESI†). As the DLs roll on the substrate under a smaller F, the number of disrupted DLs decreases.

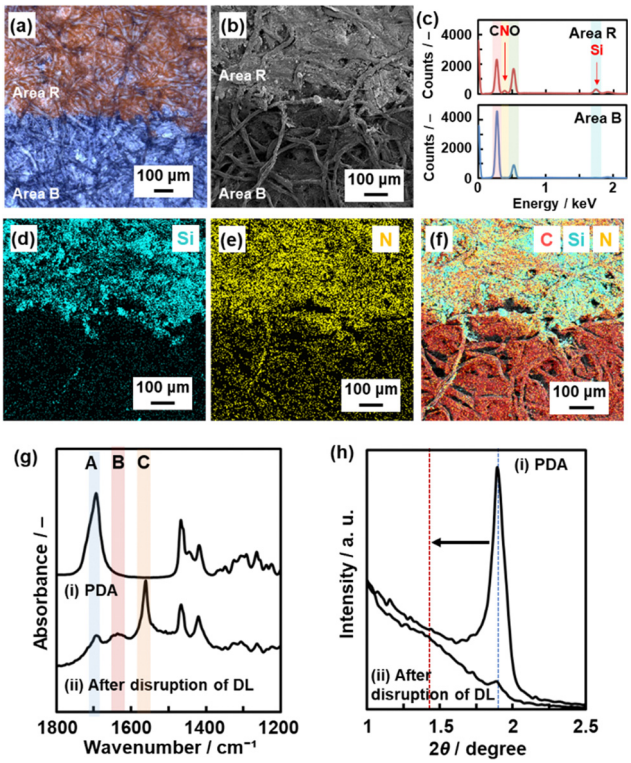

Fig. 3 PDA/DL device after the application of a weak frictional force. (a) An optical microscopy image of the interface between the color-changed (upper, area R) and original blue (lower, area B) areas. (b) SEM image. (c) EDX spectra of the areas R (upper) and B (lower). (d–f) EDX elemental mapping by Si (d), N (e), and C, Si, and N (f). (g and h) FT-IR spectra (g) and XRD patterns (h) of the pristine PDA (i) and PDA/DL after the application of friction force (ii).

PDA plays an important role in enhancing the sensitivity of visualization. The PDA/DL device on a filter paper is the same device setup as that for the detection of compression stresses in our previous work.[55] The paper-based device plays an important role in detecting the friction forces in the present work. A reference device was prepared using c-DL on a silk cloth with a rough surface (Fig. S14 in the ESI†). The sufficient disruption of DLs and outflow of the interior liquid were not observed with the application of the friction force. As the DLs are trapped in the rough substrate, the cascading response is not effectively induced by the application of the friction force. The same reference device was prepared on a polycarbonate substrate with a smooth surface. The color change with the disruption of the DLs was not observed on the smooth substrate (Fig. S14 in the ESI†). The c-DLs were removed with the sliding of the object. The results imply that a smooth substrate is preferred for the detection of compression stresses. On the other hand, a filter paper with suitable roughness is preferred for the detection of friction forces. Moreover, the surface roughness and softness have the potential for tuning the sensitivity in terms of the strength and types of the applied stresses.

On the microscopic scale, the color change proceeded with the intercalation of PEI in the interlayer space of PDA (Fig. 1d and e). The original layered PDA showed absorption corresponding to the C═O stretching vibration of the dimerized carboxy group at approximately 1700 cm^{-1} in the Fourier-transform infrared (FT-IR) spectrum (band A in Fig. 3g). After the disruption of DL on the device, the C═O stretching vibration of the carboxylate group and the N–H stretching vibration of the secondary amine salt appeared at approximately 1570 and 1640 cm^{-1}, respectively (bands B and C in Fig. 3g). The peak corresponding to the interlayer distance of the layered PDA was weakened and shifted from d_0 = 4.66 to 6.46 nm on the X-ray diffraction (XRD) pattern (Fig. 3h). The mechanoresponsive color-changing behavior of PDA was compared with that of the conventional thermoresponsive one.[41] UV-Vis spectroscopy indicated that the broadened absorption band around 600 nm shifted to the shorter wavelength region after heating at 100 °C (Fig. S15 in the ESI†). A similar peak shift was observed for the color-changed PDA in the PDA/DL device, although the original peak remained slightly unchanged. The peak shift originates

from the shortening of the effective conjugation length of PDA by molecular motion. Raman spectroscopy showed the same peak shifts as the color change after heating and exposure to the PEI solution (Fig. S15 in the ESI†). As a result, the cascading responses provided color changes in response to the weak frictional force in the range of 0.006–0.080 N. The color change of PDA in this device was irreversible. As the torsion of the conjugated main chain is caused by the intercalation of PEI in the interlayer space and subsequent distortion of the layered crystal structure, these distorted structures are irreversible and not spontaneously recovered to their original states.

2.3. Imaging and measurement of unknown friction forces

Unknown friction forces were applied to the device using a giant panda ornament (Fig. 4). Because this panda has four feet with varied contact states on the device, the frictional force applied by each foot was different (Fig. S16 in the ESI†). Here, three PDA/DL devices were set under the three feet on the table (parts A–C in Fig. 4a) because the other foot is not in contact with the table (part D in Fig. 4a). The panda was drawn along the L axis with a constant force F_s = 0.169 N and speed 6.2 ± 0.1 cm s^{-1} using a spring scale, after which the remaining DL was removed (Fig. S16 in the ESI†). The red traces on the L axis are different for parts A–C (Fig. 4b and c). The distance traverse was estimated from the traces. As compression stress was applied in the initial state before drawing (circles in Fig. 4b), the areas were removed from the analysis. As the red area was extracted from the image by trimming the blue blank space, F was estimated from the Δx value using the calibration curve in Fig. 2k (Fig. S6 in the ESI†). The measured F values were F_A = 0.114 ± 0.003 N, F_B = 0.023 ± 0.009 N, and F_C = 0.039 ± 0.002 N for parts A, B, and C, respectively (Fig. 4c and d and Fig. S16 and Table S8 in the ESI†). The sum of F_A, F_B, and F_C was 0.176 ± 0.013 N, which is consistent with the applied F_s = 0.169 N. Although the overall friction force was measured using a spring scale, the local stresses were not easy to estimate using conventional devices. Our PDA/DL device visualizes and quantifies the unknown friction forces in local areas (Fig. 4d).

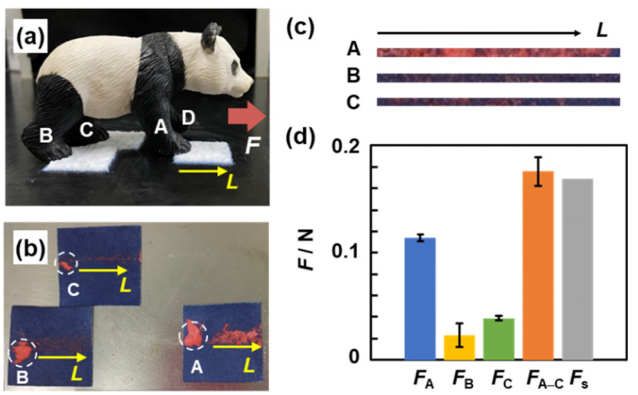

Fig. 4 Imaging and measurement of unknown weak friction forces. (a) An ornament of a giant panda set on the PDA/DL devices contacts with the feet A–C (no contact between the foot D and the device). (b) Photographs of the devices after the application of frictional force along the L axis. (c) Photographs to estimate Δx in the L axis by removing the initially contacted area (circles in panel b). (d) Estimated F of the devices contacting parts A–C (F_A, F_B, and F_C), their summation (F_{A-C} = F_A + F_B + F_C), and the actual total F measured using a spring scale (F_s).

2.4. Force mapping of handwriting in calligraphy

The device was applied for the force mapping of handwriting in calligraphy (Fig. 5). In calligraphy, characters are written using a specific ink and a brush. The word "Chemistry" is represented by two letters in Chinese (Fig. 5a). The first letter is adopted as a model for force mapping because a variety of motions, such as stopping, sweeping, and turning upward, are included in the writing processes (strokes (i)–(iv) in Fig. 5a). The proficiency of the motions determines fine or poor writing. Handwriting was performed on the PDA/DL device using a brush without ink to visualize force distribution (Fig. 5a). The same letter was written using the same brush by an expert, a practician, and a beginner three times (Fig. 5b–d and Fig. S17 in the ESI†). As a reference, they also wrote a character on paper using typical black ink. The three writers individually showed different black-color writings and red traces.

The differences in writing motion are represented by the profiles and mapping of Δx (Fig. 5e–j). For each stroke,

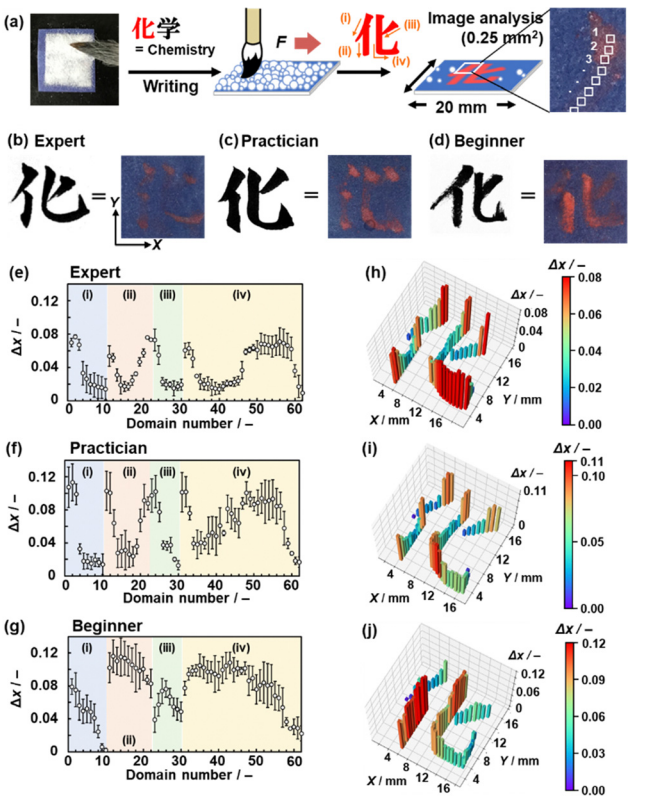

Fig. 5 Force-distribution mapping of handwriting in calligraphy. (a) Writing a Chinese character using a brush on the PDA/DL device and measuring Δx in the strokes (i)–(iv). (b–d) Photographs of the handwritten character on a paper using ink (left) and on the PDA/DL device without ink (right) by the expert (b), practician (c), and beginner (d). (e–g) Relationship between the domain numbers 1–62 and Δx in the strokes (i)–(iv) for the expert (e), practician (f), and beginner (g). (h–j) 3D force-distribution mapping for the expert (h), practician (i), and beginner (j).

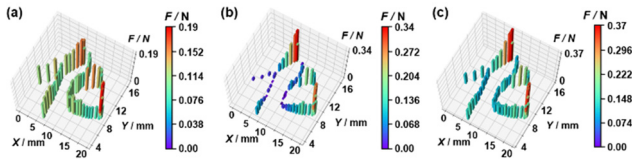

Fig. 6 Reference force-distribution imaging by the expert using a force sensor. (a) $(F_X^2 + F_Y^2)^{0.5}$. (b) F_Z. (c) $(F_X^2 + F_Y^2 + F_Z^2)^{0.5}$.

0.5 mm × 0.5 mm square domains were set to calculate the average Δx values (right panel in Fig. 5a). The strokes (i)–(iv) include 10, 12, 8, and 32 red-color domains, respectively (the horizontal axis in Fig. 5e–g and Fig. S17 in the ESI†). The relationship between the domain number and average Δx represents the force profiles for each writer (Fig. 5e–g). The relationship between the (X, Y) coordinates and Δx shows the force distribution mapping (Fig. 5h–j). Here, the color is changed by not only the friction force but also the compression stress. The motions of brush in calligraphy are exceptional cases in the present work. The motions of brush include not only lateral sliding but also vertical compression at the beginning and stop of each stroke. When the object is moved at a constant speed, in principle, only the friction force is applied to the substrate. The calibration curve in Fig. 2j and k and its application to estimate unknown F were performed by moving the object at a constant speed. In contrast, when the speed of the moving object varies, the compression stresses are also applied to the device in addition to the friction force. Both the friction and compression forces induce color changes (Δx) in the device. Only the friction force is not distinguished from the compression. In contrast, the objects were slid in the lateral direction without compressing in the vertical direction in the former demonstrations (Fig. 2 and 4). For example, as some Δx values exceeded the maximum in the range of the standard curve, *i.e.* Δx = 0.685 corresponding to F = 0.080 N in Fig. 2k (Fig. 5e–g), the measured Δx values were not simply converted to F. The number of the disrupted DLs increases with increasing F in the range of 0.006 and 0.08 N. The remaining DLs trapped inside the paper substrate are not disrupted by F larger than 0.08 N. On the other hand, the compression stresses can disrupt the trapped DLs. Therefore, the profile and mapping based on Δx represent the overall strength of the applied forces including friction and compression stresses (Fig. 5e–j).

The expert applied weak forces lower than Δx = 0.077, and the average Δx for 62 domains was 0.040 ± 0.022 (Fig. 5e and h). In contrast, the average Δx was 0.060 ± 0.031 for the practitioner and 0.076 ± 0.029 for the beginner (Fig. 5f and g). Moreover, the expert finely tuned the force of each stroke. Although a similar trend in strength was observed for the expert and practician (Fig. 5e, f, h and i), the practician applied a stronger force. On the other hand, a stronger force was constantly applied by the beginner (Fig. 5g and j). Thus, the PDA/DL device spatiotemporally visualizes the changing friction and compression stresses.

Sensing properties were studied using a force sensor as a reference (Fig. 6). A force sensor was used to analyze and copy the motions.[58] The expert wrote the character using the same brush equipped with the force sensor. Force mapping was performed in the lateral ($(F_X^2 + F_Y^2)^{0.5}$/N) and height (F_Z/N) directions (Fig. 6a and b). The total force was calculated as the sum of $(F_X^2 + F_Y^2)^{0.5}$ and F_Z (Fig. 6c). The differences in $(F_X^2 + F_Y^2)^{0.5}$ and F_Z originate from the variation in the friction coefficient caused by the deformation of the soft brush during writing (Fig. 6a and b), such as changes in the shape and contact area. When a rigid undeformed pen was used, $(F_X^2 + F_Y^2)^{0.5}$ and F_Z had similar values and trends (Fig. S18 in the ESI†). The trend of the force distribution measured using PDA/DL is not similar to that of $(F_X^2 + F_Y^2)^{0.5}$ or F_Z but to that of the total force $(F_X^2 + F_Y^2 + F_Z^2)^{0.5}$ (Fig. 5h and 6). This indicates that the PDA/DL device visualizes the force distribution including the compression and shear stresses.

The applied force to "brush" by "hand" is detected by the force sensor, whereas the actual applied force to "paper" by "brush" is detected by the PDA/DL device. In calligraphy, these measured forces are not consistent with each other. The soft brush changes the shape and contact area during the writing. The work originating from the applied force to the brush by hand is used for disruption of DLs leading to not only the color changes but also the deformation of the brush. In this manner, the PDA/DL device directly visualizes not only the frictional forces but also the overall applied forces. This new force-sensing device can be applied in a variety of fields.

3. Conclusions

A highly sensitive friction-imaging sensor was developed using a combination of PDA-coated paper and DL. The PDA/DL device visualized and measured weak frictional forces in the range of 0.006–0.080 N. Such high sensitivity was not achieved with conventional mechanoresponsive materials. The applied frictional force induces the disruption of the DLs and subsequent outflow of the interior PEI solution. The color change proceeded with the intercalation of PEI into the layered PDA coated on the paper substrate. The cascading responses enable colorimetric visualization and quantification of weak friction forces. Unknown friction forces were imaged and measured using a PDA/DL device. The irreversible color change in the device stores the information about the applied friction force in the device ensuring traceability. Moreover, the device visualized the force distribution of handwriting including the friction and compression stresses in the calligraphy. If the color-change behavior is reversible, the force mapping in the calligraphy is not achieved. The device and its design strategy can be applied as a new force sensor to understand a variety of motions. PDA can be easily coated on a variety of substrates, such as paper, glass, and polymer substrates.[48,55,56,59–61] We have developed the coating methods, such as deposition from the solution phase,[59] dipping in the precursor solution,[48,55,56] precipitation from the colloidal liquid,[60] and spraying of the precursor solution,[61] in previous works. Moreover, the stimuli responsivity was tuned by the intercalated guests in the interlayer space.[31,40,48,49,56] Therefore, similar PDA/DL devices with tunable responsivity can be prepared on a variety of substrates and substances for their wide range of applications.

Conflicts of interest

There are no conflicts to declare.

Acknowledgements

This work was partially supported by the Asahi Glass Foundation (YO), AMED (YO, JP21lm0203012j0003), the Grant-in-Aid for Scientific Research (B, 22H02148), and the Nakatani Foundation.

Notes and references

1 A. M. Malek, S. I. Alper and S. Izumo, *J. Am. Med. Assoc.*, 1999, **282**, 2035.
2 D. T. Butcher, A. Alliston and V. M. A. Weaver, *Nat. Rev. Cancer*, 2009, **9**, 108.
3 M. L. Hammock, A. Chortos, B. C. K. Tee, B. H. Tok and Z. Bao, *Adv. Mater.*, 2013, **25**, 5997.
4 Y. Zang, F. Zhang, C. Di and D. Zhu, *Mater. Horiz.*, 2015, **2**, 140.
5 L. Li, J. Zheng, J. Chne, Z. Luo, Y. Su, W. Tang, X. Gao, Y. Li, C. Cao, O. Liu, X. Kang, L. Wang and H. Li, *Adv. Mater. Interfaces*, 2020, **7**, 2000743.
6 M. Amit, L. Chukoskie, A. J. Skalsky, H. Graudadri and T. N. Ng, *Adv. Funct. Mater.*, 2020, **39**, 1905241.
7 M. M. Caruso, D. A. Davis, Q. Shen, S. A. Odomo, N. R. Sottos, S. R. White and J. S. Moore, *Chem. Rev.*, 2009, **109**, 5755.
8 A. Pucci and G. Ruggeri, *J. Mater. Chem.*, 2011, **21**, 8282.
9 Y. Sagara, S. Yamane, M. Mitani, C. Weder and T. Kato, *Adv. Mater.*, 2016, **28**, 1073.
10 P. Xue, J. Ding, P. Wang and R. Lu, *J. Mater. Chem. C*, 2016, **4**, 6688.
11 K. M. Herbert, S. Schretti, S. J. Rowan and C. Weder, *Macromolecules*, 2017, **60**, 8846.
12 J. Zhao, Z. Chi, Y. Zhang, Z. Mao, Z. Yang, E. Ubba and Z. Chi, *J. Mater. Chem. C*, 2018, **6**, 6327.
13 H. Traeger, D. J. Kiebala, C. Weder and S. Schrettl, *Macromol. Rapid Commun.*, 2020, **42**, 2000573.
14 T. Seki, N. Hoshino, Y. Suzuki and S. Hayashi, *CrystEngComm*, 2021, **23**, 5686.
15 B. Das, S. Jo, J. Zheng, J. Chen and K. Sugihara, *Nanoscale*, 2022, **14**, 1670.
16 K. Ariga, *Small Methods*, 2022, **6**, 2101577.
17 L. Veeramuthu, C. J. Cho, M. Venkatesan, R. Kumar, H. Y. Hsu, B. X. Zhuo, L. J. Kau, M. A. Chung, W. Y. Lee and C. C. Kuo, *Nano Energy*, 2022, **101**, 107592.
18 Z. Wang, Z. Ding, Y. Yang, L. Hu, W. Wu, Y. Gao, Y. Wei, X. Zhang and G. Jiang, *Chem. Eng. J.*, 2023, **457**, 141293.
19 W. C. Han, Y. J. Lee, S. U. Kim, H. J. Lee, Y. S. Kim and D. S. Kim, *Small*, 2023, **19**, 2206299.
20 D. H. Jiang, Y. C. Liao, C. J. Cho, L. Verramuthu, F. C. Liang, T. C. Wang, C. C. Chueh, T. Satoh, S. H. Tung and C. C. Kuo, *ACS Appl. Mater. Interfaces*, 2020, **12**, 14408.
21 Y. Sagara, T. Mutai, I. Yoshikawa and K. Araki, *J. Am. Chem. Soc.*, 2007, **129**, 1520.
22 J. Kunzelman, M. Kinami, B. R. Creshaw, J. D. Protasiewicz and C. Weder, *Adv. Mater.*, 2008, **20**, 119.
23 G. Zhang, J. Lu, M. Sabat and C. Fraser, *J. Am. Chem. Soc.*, 2010, **132**, 2160.
24 K. Nagura, S. Saito, H. Yusa, H. Yamawaki, H. Fujihisa, H. Sato, Y. Shimoikeda and S. Yamaguchi, *J. Am. Chem. Soc.*, 2013, **135**, 10322.
25 T. Seki, Y. Takamatsu and H. Ito, *J. Am. Chem. Soc.*, 2016, **138**, 6252.
26 M. Okazaki, Y. Takeda, P. Data, P. Pander, H. Higginbotham, A. P. Monkman and S. Minakata, *Chem. Sci.*, 2017, **8**, 2677.
27 B. Poggi, L. Bodelot, M. Louis, R. Métivier and C. Allain, *J. Mater. Chem. C*, 2021, **9**, 12111.
28 D. J. Ahn, S. Lee and J. M. Kim, *Adv. Funct. Mater.*, 2009, **19**, 1483.
29 O. Yarigama, J. Jaworski, B. Yoon and J. M. Kim, *Chem. Commun.*, 2012, **48**, 2469.
30 X. Qian and B. Städler, *Chem. Mater.*, 2019, **31**, 1196.
31 Y. Oaki, *Chem. Commun.*, 2020, **56**, 13069.
32 R. Jelinek and M. Ritenberg, *RSC Adv.*, 2013, **3**, 21192.
33 J. Huo, Q. Deng, T. Fan, G. He, X. Hu, X. Hong, H. Chen, S. Luo, Z. Wang and D. Chen, *Polym. Chem.*, 2017, **8**, 7438.
34 M. Weston, A. D. Tjandra and R. Chandrawati, *Polym. Chem.*, 2020, **11**, 166.
35 B. Hu, S. Sun, B. Wu and P. Wu, *Small*, 2019, **15**, 1804975.
36 N. Phonchai, C. Khanantong, F. Kielar, R. Traiphol and N. Traiphol, *ACS Appl. Nano Mater.*, 2019, **2**, 4489.
37 G. Shin, M. I. Khazi and J. M. Kim, *Macromolecules*, 2020, **53**, 149.
38 R. Bisht, V. Dhyani and R. Jelinek, *Adv. Opt. Mater.*, 2021, **9**, 2001497.
39 J. Park, J. M. Heo, S. Seong, J. Noh and J. M. Kim, *Nat. Commun.*, 2021, **2**, 4207.
40 Y. Ishijima, H. Imai and Y. Oaki, *Chem*, 2017, **3**, 509.
41 M. Nakamitsu, H. Imai and Y. Oaki, *ACS Sens.*, 2020, **5**, 133.
42 K. Watanabe, H. Imai and Y. Oaki, *Small*, 2020, **16**, 2004586.
43 R. W. Carpick, D. Y. Sasaki and A. R. Burns, *Langmuir*, 2000, **16**, 1270.
44 H. Feng, J. Lu, J. Li, F. Tsow, E. Forzani and N. Tao, *Adv. Mater.*, 2013, **25**, 1729.
45 D. H. Park, J. Hong, I. S. Park, C. W. Lee and J. M. Kim, *Adv. Funct. Mater.*, 2014, **24**, 5186.
46 J. P. Lee, H. Hwang, S. Chae and J. M. Kim, *Chem. Commun.*, 2019, **55**, 9395.
47 Q. Li, Y. X. Wang and Y. Chen, *ACS Macro Lett.*, 2022, **11**, 103.
48 H. Terada, H. Imai and Y. Oaki, *Adv. Mater.*, 2018, **30**, 1801121.
49 K. Watanabe, H. Imai and Y. Oaki, *J. Mater. Chem. C*, 2020, **8**, 1265.
50 F. Yang, X. Li and Y. Chen, *Adv. Opt. Mater.*, 2022, **10**, 2102552.
51 L. Juhasz, R. D. Ortuso and K. Sugihara, *Nano Lett.*, 2021, **21**, 543.
52 L. Polacchi, A. Brosseau, R. Métivier and C. Allain, *Chem. Commun.*, 2019, **55**, 14566.

53 B. P. Binks and R. Murakami, *Nat. Mater.*, 2006 **5**, 865.
54 K. Kido, T. Sumoto, Y. Yasui, Y. Nakamura and S. Fujii, *Adv. Powd. Technol.*, 2017, **28**, 1977.
55 M. Nakamitsu, K. Oyama, H. Imai, S. Fujii and Y. Oaki, *Adv. Mater.*, 2021, **33**, 2008755.
56 M. Takeuchi, H. Imai and Y. Oaki, *ACS Appl. Mater. Interfaces*, 2017, **9**, 16546.
57 E. Reinhard, W. Heidrich, P. Debevec, S. Pattanaik, G. Ward and K. Myszkowski, *High Dynamic Range Imaging: Acquisition, Display, and Image-Based Lighting*, Elsevier Science, Saint Louis, 2nd edn, 2010, ch. 2, p. 35.
58 K. Miura, A. Matsui and S. Katsura, *IEEE/ASME Trans. Mechatronics*, 2016, **21**, 1015.
59 M. Okaniwa, Y. Oaki, S. Kaneko, K. Ishida, H. Maki and H. Imai, *Chem. Mater.*, 2015, **27**, 2627.
60 N. Shioda, J. M. Heo, B. Kim, H. Imai, J. M. Kim and Y. Oaki, *Sens. Diagn.*, 2022, **1**, 160.
61 A. Edagawa, S. Matsuda, H. Kawakubo, H. Imai and Y. Oaki, *ACS Appl. Mater. Interfaces*, 2022, **14**, 43792.

